Particuology 115 (2026) 366–377

Contents lists available at ScienceDirect

Particuology

journal homepage: www.elsevier.com/locate/partic

# Kinetic modeling of methyl methacrylate gas-phase decomposition and its impact on polymethyl methacrylate pyrolysis yields

Stefan Pielsticker*, Konstantinos Gfall, Wilko Rohlfs, Reinhold Kneer

*Institute of Heat and Mass Transfer (WSA), RWTH Aachen University, Augustinerbach 6, 52056, Aachen, Germany*

## HIGHLIGHTS

- Separate MMA kinetic modeling is undertaken to improve PMMA pyrolysis models.
- Low-energy decarboxylation dominates cracking reactions at low temperatures.
- Competitive reaction model (CRM) accurately predicts MMA product selectivity.
- Direct solid-to-gas pathways are key to predict low-temperature PMMA yields.
- Peak monomer recovery near 723 K shows excellent agreement with literature.

## GRAPHICAL ABSTRACT

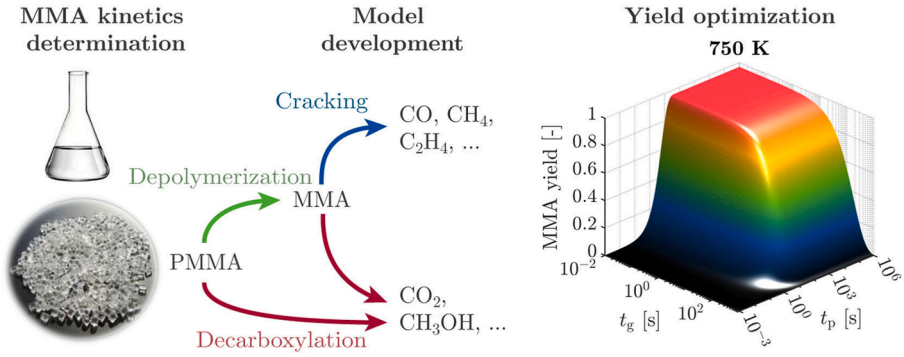


## ARTICLE INFO

*Keywords:*
MMA and PMMA pyrolysis
Fluidized bed reactor
FTIR gas analysis
Kinetic modelling
Primary and secondary reactions

## ABSTRACT

Chemical recycling of polymethyl methacrylate (PMMA) to its monomer, methyl methacrylate (MMA), requires balancing primary depolymerization with the suppression of secondary gas-phase reactions. This study investigates non-oxidative MMA decomposition in a fluidized bed reactor across a temperature range of 623 to 1073 K using online FTIR spectroscopy. Experimental results reveal a significant shift in product selectivity: low temperatures favor a low-energy decarboxylation pathway (yielding $CO_2$ and methanol), while high temperatures promote radical cracking (yielding CO and light hydrocarbons). To describe this, a two-competing-reactions model (CRM) is used, outperforming the traditional single first-order approaches. The CRM identifies two distinct activation energies: $E_{a,1} = 76.5$ kJ mol$^{-1}$ for decarboxylation and $E_{a,2} = 269.9$ kJ mol$^{-1}$ for cracking. The research further demonstrates that the classical sequential decomposition model (PMMA → MMA → light gases) overpredicts monomer yields at low temperatures. By integrating a direct solid-to-gas pathway to account for side-chain break-off and incorporating multi-volume reactor hydrodynamics, the model's predictive accuracy significantly improved. This integrated framework identifies an optimal recovery window near 723 K, achieving MMA yields over 95 %.

This article is part of a special issue entitled: Reactive Particle-Gas Systems II published in Particuology.

* Corresponding author.
*E-mail address:* pielsticker@wsa.rwth-aachen.de (S. Pielsticker).

https://doi.org/10.1016/j.partic.2026.05.011
Received 12 January 2026; Received in revised form 13 May 2026; Accepted 17 May 2026
Available online 28 May 2026

## 1. Introduction

The growing challenge of global plastic waste disposal, with annual polymer production exceeding 460 million tons in 2021 (OECD, 2022), requires a rapid transition to sustainable circular economy strategies. Among these strategies, chemical recycling through thermal depolymerization offers a promising path, as this enables the recovery of the original monomers, which can then be repolymerized into virgin-quality materials (Achilias, 2007; Braido et al., 2018; Gkaliou et al., 2023; Kikuchi et al., 2014). Polymethyl methacrylate (PMMA) is a prominent candidate for this process, as the chemical structure allows a breakdown into the monomer methyl methacrylate (MMA) (dos Santos et al., 2022). Multiple studies have reported MMA yields around 95 % or more (Ferreira et al., 2025; Kaminsky & Franck, 1991; Kang et al., 2008). Given the need for high throughput, good heat transfer, and the necessary reaction time, fluidized bed reactors (FBR) are considered the preferred technology for the depolymerization of PMMA on an industrial scale (Ferreira et al., 2025; Kaminsky & Franck, 1991; Smolders & Baeyens, 2004).

The process requires a dynamic balance between two competing objectives: first, maximizing the rate of primary solid-phase decomposition of PMMA into MMA monomer, and second, suppressing the subsequent thermal destruction of the volatile MMA monomer in the gas phase (secondary decomposition). The primary decomposition has been intensively studied, and multiple influencing factors have been identified, e.g., temperature (Ferreira et al., 2025; Kaminsky & Franck, 1991; Kang et al., 2008; Pielsticker et al., 2025), heating rate (Ferriol et al., 2003; Korobeinichev et al., 2019), molecular weight (Arisawa & Brill, 1997; Holland & Hay, 2001), polymerization method (Kashiwagi et al., 1986), or additional catalytic materials (Chub et al., 2022; Nguyen et al., 2026). The thermal decomposition of PMMA primarily occurs through a radical depolymerization (unzipping) mechanism, where the polymer chains break down into their original methyl methacrylate (MMA) monomers (Arisawa & Brill, 1997). This process is triggered by two main initiation pathways: chain-end scission at lower temperatures (approximately 523−573 K) involving weak terminal linkages, and random scission within the polymer backbone at higher temperatures (approximately 623−723 K) (Arisawa & Brill, 1997). Once initiated, the radical unzips through the chain, successively releasing monomers until the reaction is stopped by a termination step like disproportionation or recombination. The released monomer units are further decomposed in the gas phase to smaller molecules. Although many studies mention the gas-phase reaction as a factor reducing the MMA yield (Ferreira et al., 2025; Kaminsky & Franck, 1991), the separate MMA decomposition is mostly studied in the context of oxidative reactions (Dakshnamurthy et al., 2019; Zeng et al., 2002), while data on pure non-oxidative MMA decomposition is scarce (Blanco et al., 2014; Sanders et al., 2023). Thus, in the context of monomer recycling for a circular economy, investigating the interplay of primary and secondary reactions is of high importance (dos Santos et al., 2022).

Consequently, in this study, a detailed experimental investigation of pure methyl methacrylate (MMA) decomposition in a non-oxidative environment under industrially relevant conditions is undertaken. The decomposition products are measured time-resolved with a previously calibrated Fourier-transform infrared spectrometer (Pielsticker et al., 2025). Based on these data, a comprehensive kinetic framework featuring a two-competing-reactions model to mechanistically resolve the temperature-dependent selectivity of MMA decomposition will be developed. Additionally, the typically used single first-order approach for PMMA decomposition (Arisawa & Brill, 1997) will be extended by an additional pathway to directly produce light gases, reflecting the chain-end scission at lower temperatures. This final chemical kinetic framework will then be coupled with reactor hydrodynamics modeling to gain insights into the effects of gas residence time distributions on the prediction and optimization of monomer recovery.

## 2. Experimental investigation

For the experimental investigations, a lab-scale reactor setup in two slightly different modifications is used. In both configurations, the reaction temperature ($T_R = 623-1073$ K) is set via an electrically heated furnace, where the reactor is placed.

### 2.1. MMA pyrolysis

To solely investigate the decomposition of the monomer methyl methacrylate (MMA) in the gas phase, the setup depicted in Fig. 1 is used. In this modification, the $N_2$ stream is split into two sub-streams: one passing the annular gap between the two ceramic pipes and the other dosing the MMA into the reactor.

The dosing gas flow first bubbles through a tempered bath (293 K) of liquid MMA before passing a water-operated cooler. Via visual observation and a dew point sensor, saturation with MMA in the gas stream at the cooler outlet is ensured. By using the Antoine equation with coefficients provided from the NIST database (NIST Chemistry WebBook, 2023) and originally determined based on experimental data from Brockhaus and Jenckel (1956), the saturation pressure $p_s$ is estimated according to

$$\log_{10}(p_s) = 5.37785 - \frac{1945.56\,\mathrm{K}}{T_s - 7.569\,\mathrm{K}}, \tag{1}$$

while the measured gas outlet temperature of 284 K is assumed as the saturation temperature $T_s$. After leaving the cooler, the gas stream is heated to prevent recondensation of the MMA. By assuming the ideal gas law, the volume fraction $\varphi_{MMA}$ of MMA in the feed gas flow can be calculated:

$$\varphi_{MMA,feed} = \frac{p_s(T)}{p}. \tag{2}$$

The total pressure $p$ is approximately the reactor pressure $p = 1.113$ bar neglecting the pressure loss from the cooler to the reactor. The applicability of this procedure has already been successfully demonstrated in a previous study (Pielsticker et al., 2025). Afterward, the stream is guided through a small ceramic pipe to the bottom of the FBR and mixes with the fluidization volume flow. Neglecting decomposition in the small ceramic feed pipe, the initial volume fraction at the reactor bottom is given as

$$\varphi_{MMA,0} = \frac{\varphi_{MMA,feed}}{1 - \varphi_{MMA,feed}} \cdot \frac{\dot{V}_{N_2,feed}}{\dot{V}_{N_2,feed} + \dot{V}_{N_2,fl}}, \tag{3}$$

when the $N_2$ flows from the feed ($\dot{V}_{N_2,feed}$) and the fluidization ($\dot{V}_{N_2,fl}$) mix. For all experiments, the ratio of $N_2$ flow passing through the system feed compared to the total $N_2$ gas flow is kept constant at a ratio of 1:10. Regardless of the total volume flow, the initial MMA volume fraction is set to $\varphi_{MMA,0} = 1.9$ %. This volume fraction falls well into the range of previously recorded reference spectra for MMA (Pielsticker et al., 2024). By changing the total volume flow between 50 and 150 $l_n\ h^{-1}$, the gas residence time in the reactor is varied between 6 and 18 s. The reactor temperature $T_R$ at the bottom is controlled with an S-type thermocouple.

The total gas stream leaves the reactor through the reactor head at the top and is afterward guided through heated pipes (453 K) and a fine filter to a Fourier-transform infrared (FTIR) spectrometer. The heated pipes avoid condensation of formed reaction products and MMA before the FTIR gas cell. The FTIR is an Ansyco GASMET DX-2000 equipped with a heated gas cell (2.0 m optical path length, 453 K and 220 ml volume) that captures spectra with a frequency of 0.38 Hz in the mid-infrared wavenumber region $\nu = 600-4200\ cm^{-1}$ at a spectral resolution of 8 $cm^{-1}$. In total, the volume fractions $\varphi_{i,FTIR,}$ of 13 relevant gas species including MMA ($C_5H_8O_2$), carbon monoxide (CO), carbon

dioxide ($CO_2$), methane ($CH_4$), benzene ($C_6H_6$), ethylene ($C_2H_4$), ethane ($C_2H_6$), propylene ($C_3H_6$), propane ($C_3H_8$), butane ($C_4H_{10}$), formaldehyde ($CH_2O$), methanol ($CH_3OH$) and ethanol ($C_2H_5OH$), are quantitatively determined. For each experimental condition (varied temperature and volume flow), first, a steady state is awaited before the volume fraction is measured over a period of at least 15 min and then averaged.

Based on a mass balance around the reactor system, the mass-specific yield $y_i$ of each species in relation to the injected MMA mass (in $kg_i$ per $kg_{MMA}$) can be expressed as:

$$y_i = \frac{M_i \cdot \varphi_{i,FTIR}}{M_{MMA} \cdot \varphi_{MMA,0}}. \quad (4)$$

### 2.2. PMMA pyrolysis

The pyrolytic decomposition of solid PMMA particles has been the focus of a previous study (Pielsticker et al., 2026). Compared to the setup used for the MMA pyrolysis, slight modifications are considered as illustrated in Fig. 2.

The continuous MMA fuel feed system was replaced by a lock system to batch-wise inject solid fuel samples ($m_{PMMA}$ = 15 mg, $d_p$ = 600–800 µm) in a discontinuous procedure. The PMMA particles fall driven by gravity and an additional purge gas flow to the bottom of the reactor, where they mix with a fluidized bed consisting of inert $Al_2O_3$ particles (true density 3216 kg $m^{-3}$). The bed particles are in the size range 100–180 µm and account for a total mass of approximately 90 g and a fixed bed height of 29 mm. The minimum fluidization velocity for those particles was measured with a cold transparent 1:1 demonstrator to be 0.009 m $s^{-1}$. The fluidization gas flow of 80 $l_n$ $h^{-1}$ (standard conditions) correlates with a free-flow velocity of 0.02–0.037 m $s^{-1}$ and yields in a fluidized bed with a bed expansion between 12 and 25 %. The bed is categorized as being in the bubbling regime, typical for the used particles of Geldart type B (Geldart, 1973; Kunii & Levenspiel, 1997). Mixing characteristics were also validated in the cold-flow transparent demonstrator. Despite the density disparity between the bed ($Al_2O_3$) and fuel particles (PMMA), the bubbling fluidization regime maintained a uniform spatial distribution of the fuel throughout the bed height, preventing segregation at the bed surface. The bed temperature $T_{FB}$ is controlled with an S-type thermocouple. The bed serves as a thermal reservoir that provides the energy required for the strongly endothermic depolymerization reaction and ensures nearly isothermal conditions by minimizing temperature fluctuations during the solid-to-gas conversion.

While the particles remain in the reactor until complete decomposition, the gaseous reaction products, fluidization gas, and purge gas mix with each other and leave the reaction zone via an exhaust gas pipe. The significantly smaller pipe diameter of the exhaust pipe in the PMMA experiments shortens the gas residence time to approximately 6–8 s. Similar to the MMA experiments, the composition of the exhaust gas stream was measured with the FTIR spectrometer with the same configuration.

For the batch experiments of PMMA, the observed release rate is given by Eq. (5)

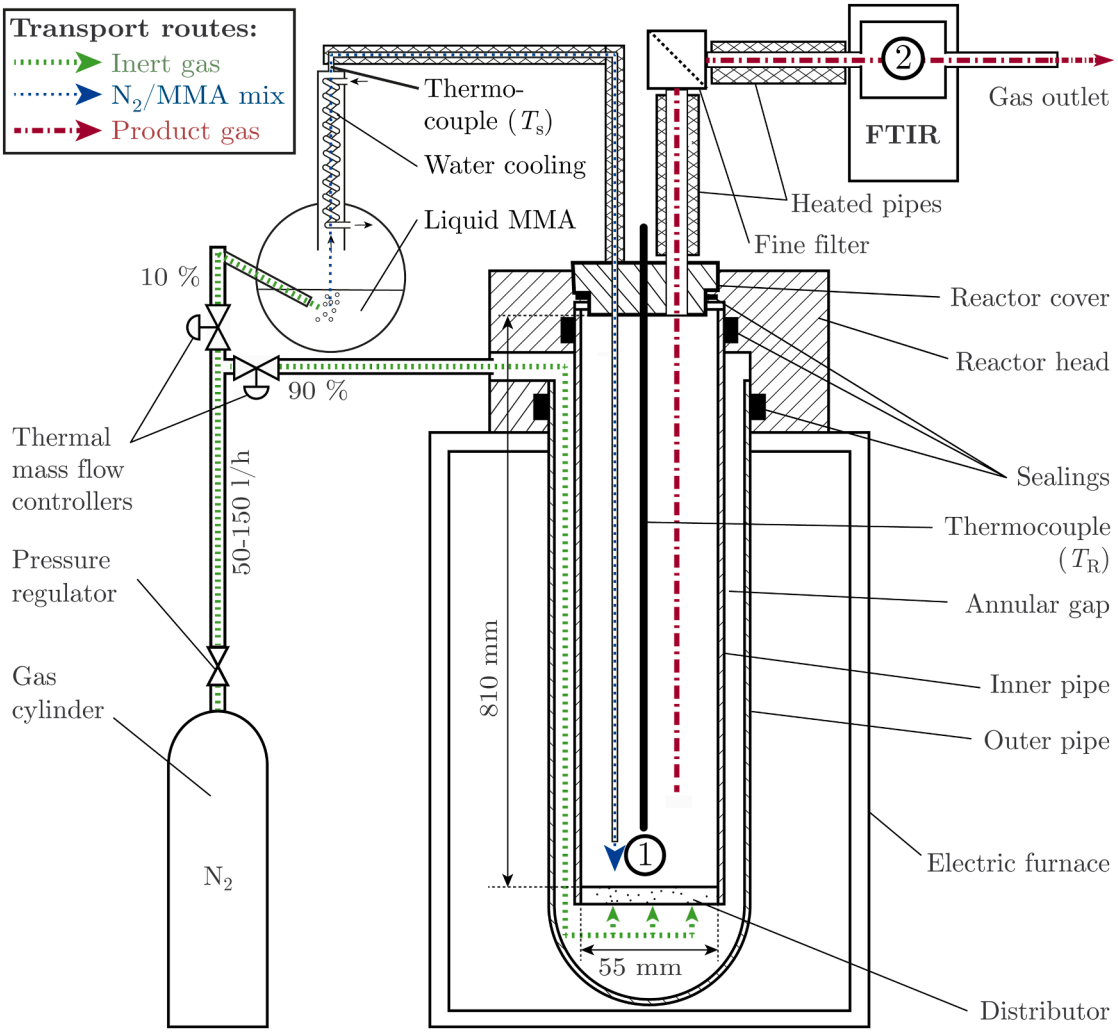


**Fig. 1.** Experimental setup for MMA pyrolysis.

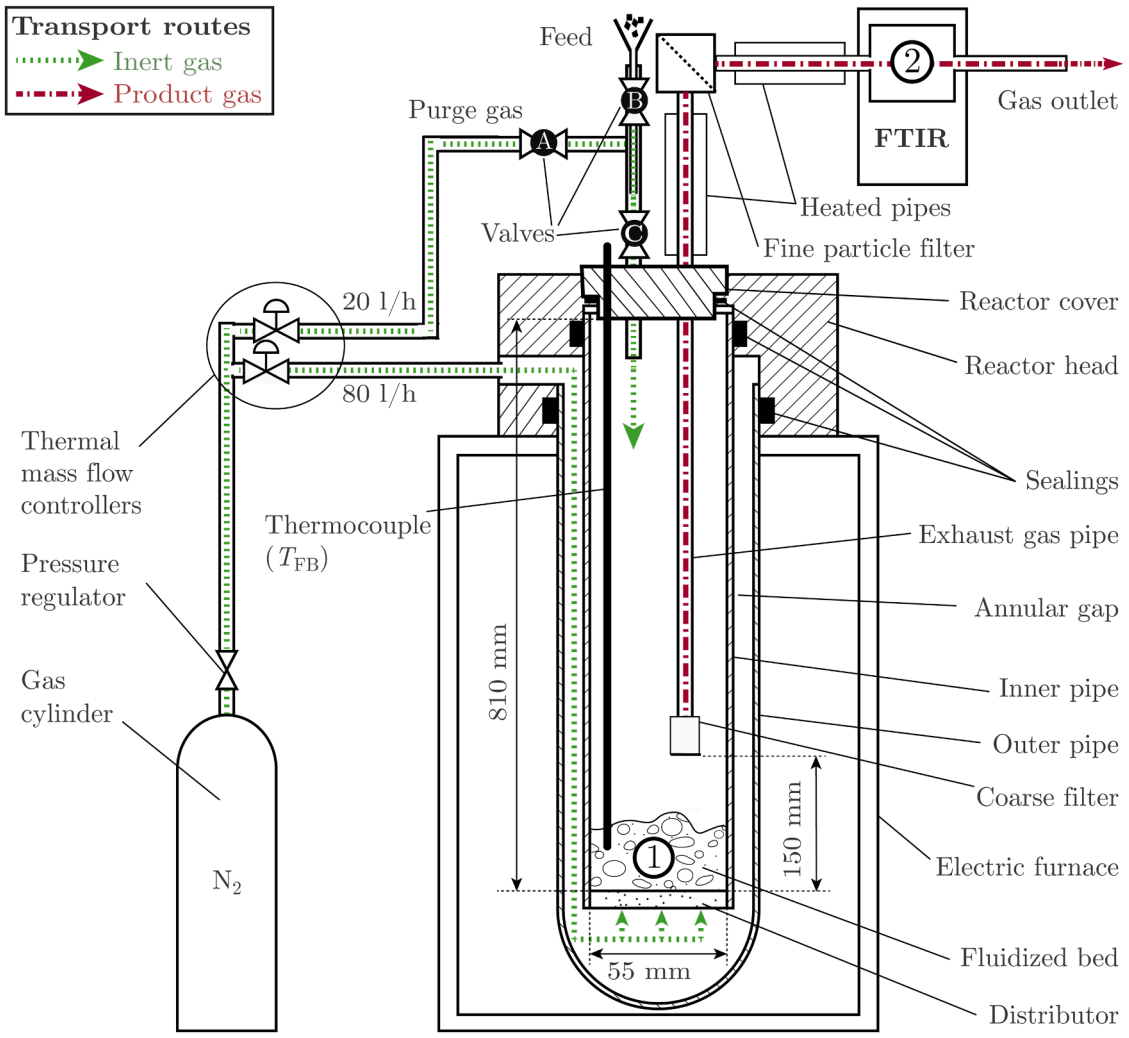


**Fig. 2.** Experimental setup for PMMA pyrolysis in a fluidized bed reactor (Gfall et al., 2025).

**Table 1**
Mass-specific yields of different product species resulting from MMA pyrolysis at different reactor temperatures and gas volume flows (in $kg_i$ per $kg_{MMA}$).

| Temp. [K] | Vol. flow [$l_n\ h^{-1}$] | $CO_2$ | CO | $CH_4$ | $C_2H_6$ | $C_2H_4$ | $C_3H_8$ | $C_3H_6$ | $C_4H_{10}$ | $CH_2O$ | $CH_4O$ | $C_2H_6O$ | $C_6H_6$ | $C_5H_8O_2$ |
|---|---|---|---|---|---|---|---|---|---|---|---|---|---|---|
| 773 | 50 | 0.0495 | 0.0076 | 0.0005 | 0.0033 | 0.0003 | 0.0009 | — | 0.0003 | 0.0062 | 0.0137 | 0.0032 | 0.0054 | 0.9091 |
| 773 | 100 | 0.0178 | 0.0033 | 0.0004 | 0.0016 | $< 10^{-4}$ | 0.0008 | — | 0.0004 | 0.0038 | 0.0091 | 0.0026 | 0.0039 | 0.9562 |
| 773 | 150 | 0.0023 | 0.0009 | $< 10^{-4}$ | 0.0004 | $< 10^{-4}$ | $< 10^{-4}$ | $< 10^{-4}$ | $< 10^{-4}$ | 0.0016 | 0.0046 | 0.0026 | 0.0023 | 0.9849 |
| 823 | 50 | 0.0501 | 0.0373 | 0.0040 | 0.0043 | 0.0008 | 0.0001 | 0.0179 | 0.0008 | 0.0191 | 0.0116 | 0.0115 | 0.0037 | 0.8387 |
| 823 | 100 | 0.0095 | 0.0140 | 0.0023 | 0.0037 | 0.0004 | 0.0003 | 0.0022 | 0.0012 | 0.0100 | 0.0070 | 0.0081 | 0.0050 | 0.9362 |
| 823 | 150 | 0.0059 | 0.0068 | 0.0007 | 0.0013 | 0.0004 | $< 10^{-4}$ | 0.0007 | 0.0004 | 0.0055 | 0.0041 | 0.0065 | 0.0058 | 0.9618 |
| 873 | 50 | 0.1120 | 0.1937 | 0.0132 | 0.0017 | 0.0083 | — | 0.0693 | — | 0.0479 | 0.0060 | 0.0180 | 0.0034 | 0.5266 |
| 873 | 100 | 0.0223 | 0.1142 | 0.0092 | 0.0066 | 0.0026 | — | 0.0694 | — | 0.0395 | 0.0061 | 0.0195 | 0.0032 | 0.7075 |
| 873 | 150 | 0.0008 | 0.0578 | 0.0025 | 0.0032 | $< 10^{-4}$ | — | 0.0269 | — | 0.0261 | 0.0032 | 0.0141 | 0.0026 | 0.8629 |
| 908 | 50 | 0.1306 | 0.3704 | 0.0452 | 0.0003 | 0.0400 | — | 0.1476 | — | 0.0475 | 0.0033 | 0.0117 | 0.0103 | 0.1930 |
| 908 | 100 | 0.0212 | 0.2444 | 0.0174 | $< 10^{-4}$ | 0.0184 | — | 0.1026 | — | 0.0633 | — | 0.0144 | 0.0098 | 0.5084 |
| 908 | 150 | — | 0.1824 | 0.0098 | 0.0005 | 0.0078 | — | 0.0529 | — | 0.0565 | $< 10^{-4}$ | 0.0138 | 0.0077 | 0.6705 |
| 943 | 50 | 0.1867 | 0.3912 | 0.1074 | 0.0039 | 0.1005 | — | 0.1178 | — | 0.0209 | 0.0004 | 0.0050 | 0.0348 | 0.0314 |
| 943 | 100 | 0.0783 | 0.4236 | 0.0995 | 0.0035 | 0.0944 | — | 0.1578 | — | 0.0320 | 0.0030 | 0.0065 | 0.0314 | 0.0700 |
| 943 | 150 | 0.0399 | 0.4109 | 0.0686 | 0.0021 | 0.0631 | — | 0.1734 | — | 0.0447 | 0.0041 | 0.0108 | 0.0195 | 0.1627 |
| 973 | 50 | 0.2081 | 0.3973 | 0.1253 | 0.0025 | 0.1144 | — | 0.0693 | — | 0.0075 | 0.0005 | 0.0041 | 0.0522 | 0.0188 |
| 973 | 100 | 0.1350 | 0.4163 | 0.1249 | 0.0018 | 0.1193 | — | 0.0958 | — | 0.0129 | 0.0004 | 0.0053 | 0.0534 | 0.0349 |
| 973 | 150 | 0.1054 | 0.4175 | 0.1169 | 0.0015 | 0.1138 | — | 0.1060 | — | 0.0148 | $< 10^{-4}$ | 0.0069 | 0.0512 | 0.0659 |

$$\frac{dy_i}{dt} = \frac{\rho_{N_2} \cdot M_i}{M_{N_2}} \cdot \frac{\dot{V}_{fl} + \dot{V}_{purge}}{m_{PMMA}} \cdot \frac{\varphi_i(t)}{1 - \sum_{j=1}^{13} \varphi_j(t)}. \quad (5)$$

However, the observed release rates do not directly reflect the behavior at the particle level but include effects of the gas transport and mixing between the reaction zone and the FTIR gas analysis. To compensate for those effects, a convolution procedure based on the methods proposed by Abad et al. (2005) is undertaken as explained in detail in the study by Pielsticker et al. (2019) for biomass.

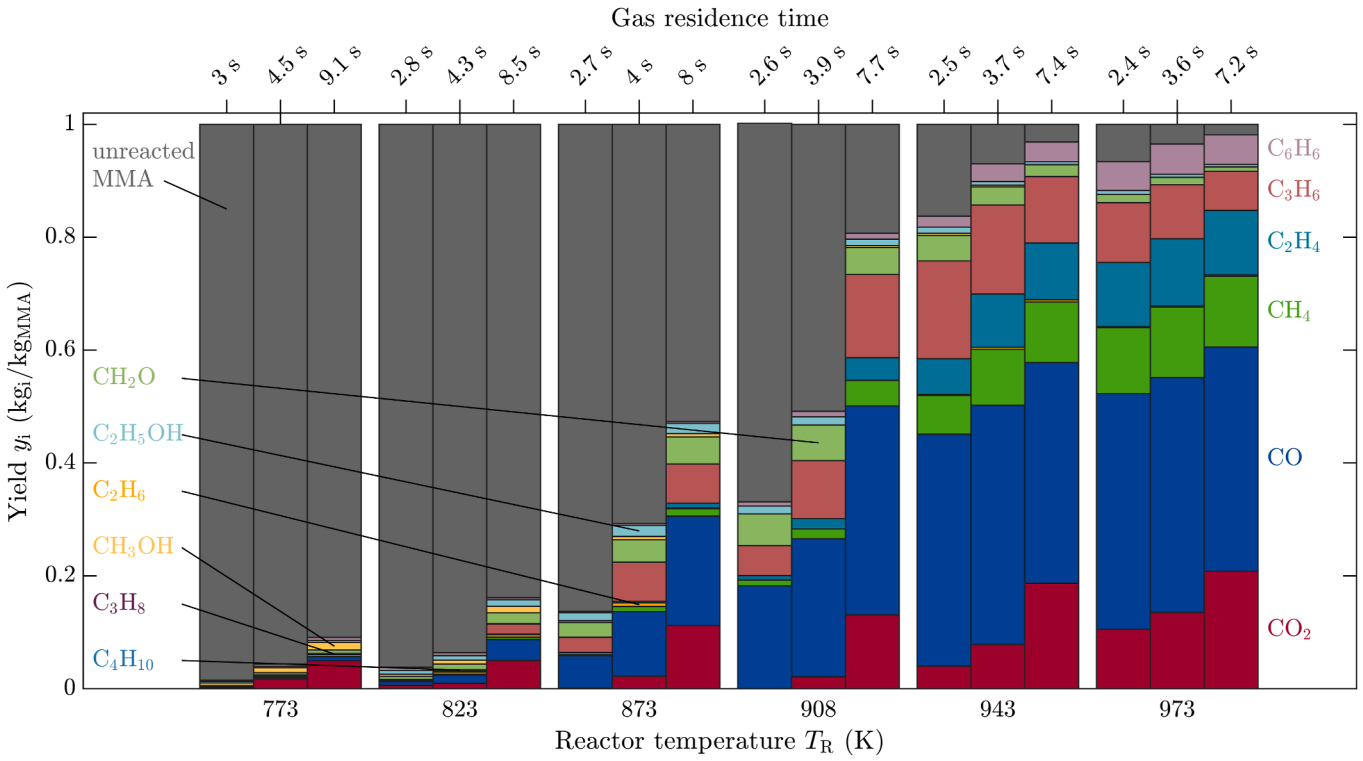


**Fig. 3.** Decomposition products of MMA during pyrolysis in $N_2$ for different reactor temperatures and gas flow rates resulting in gas residence times printed above.

## 3. Results

This section will first present a detailed experimental investigation into the gas-phase pyrolysis of methyl methacrylate (MMA) across a broad temperature range to elucidate the secondary decomposition reactions. Building upon these findings, a kinetic modeling framework is then developed to accurately describe the interplay between gas-phase chemistry and primary particle decomposition kinetics by identifying key competing reaction pathways that govern the product distribution. Finally, the derived kinetic model is integrated into a comprehensive reactor model to simulate the overall process, providing a robust prediction of the PMMA monomer recovery.

### 3.1. Experimental investigation of MMA decomposition

Experiments with pure MMA as an educt serve to determine the gas-phase reaction kinetics. Table 1 and Fig. 3 show the yields of light gas decomposition products and the remaining part of unreacted MMA at different temperatures $T_R$ and volume flows $\dot{V}$. Changing the volume flow allows for the investigation of different gas residence times at the same temperature. Overall, as expected, higher temperatures and longer residence times promote the decomposition of MMA into smaller light gas fragments.

The light gas composition reveals a significant shift in the product spectrum as temperature increases. At low temperatures, the spectrum is dominated by $CO_2$, signaling a lower-energy decarboxylation pathway. This is accompanied by oxygenated fragments like methanol ($CH_3OH$) and formaldehyde ($CH_2O$), confirming the initial instability of the ester group (Moens et al., 2020). While ethane ($C_2H_6$) is present, its relatively low and steady yield suggests that methyl radical recombination is a minor pathway compared to primary scission.

At higher temperatures, the CO yield surpasses that of $CO_2$, indicating the onset of non-selective carbonyl bond cleavage (Kaminsky & Franck, 1991). The intense thermal cracking is marked by a sharp rise in methane ($CH_4$) and ethylene ($C_2H_4$). Interestingly, propylene ($C_3H_6$) reaches a maximum near 943 K before declining at 973 K, suggesting that at extreme temperatures, even these primary segments undergo secondary cracking into smaller fragments or contribute to the formation of benzene ($C_6H_6$). Contrary to lower-temperature stability, the disappearance of butane ($C_4H_{10}$) above 823 K indicates that high-severity regimes favor unimolecular cracking over the bimolecular recombination of larger radicals. The sustained yields of benzene at 973 K suggest that the reactor environment facilitates cyclization and aromatization of unsaturated $C_2$ and $C_3$ intermediates rather than alkane recombination.

Research utilizing shock tube studies for MMA pyrolysis, although conducted at significantly higher temperatures (1200−1600 K), identified CO, $CO_2$, and $CH_2O$ as the main decomposition fragments (Sanders et al., 2023). The current FBR experiments, operating up to 973 K, reveal these same products, demonstrating that the kinetic pathways initiated in the FBR vapor phase are fundamentally analogous to those governing high-temperature gas-phase cracking (Sanders et al., 2023).

### 3.2. Determination of kinetic parameters for MMA gas-phase decomposition

To describe the observed decomposition behavior, various kinetic models were evaluated to determine the governing kinetic parameters. In all modeling approaches, the reactor was characterized as an ideal plug-flow reactor (PFR). The ideal PFR model assumes a uniform velocity profile where radial mixing is instantaneous and axial backmixing is non-existent. Under these conditions, every fluid element experiences an identical residence time, effectively behaving as an infinitesimal batch reactor progressing through the pipe. While the PFR model provides a robust mathematical framework, real tubular reactors – especially those operating under laminar flow conditions – deviate from ideality due to the parabolic velocity profile. This results in a broader residence time distribution and typically lower conversion rates compared to the ideal case. To bridge the gap between the simplified PFR model and the experimental observations, an effective reactor volume $V_{eff}$ is implemented to account for several experimental factors.

This approach provides necessary hydrodynamic compensation by addressing the kinetic inefficiencies introduced by non-ideal flow patterns and the lack of perfect axial uniformity. Furthermore, the use of an effective volume allows for the integration of the effect of an axial temperature profile:

$$V_{\mathrm{eff}} = \frac{\pi \cdot d_{\mathrm{R}} \cdot \int_0^L r(T(x))\, dx}{4 \cdot \eta \cdot r(T_{\mathrm{R}})}. \tag{6}$$

The effective reactor volume is calculated by integrating the temperature-dependent reaction rate $r(T)$ along the entire reactor length and setting this into relation to the reaction rate $r(T_{\mathrm{R}})$ at the reactor maximum temperature located at the bottom. The axial temperature profile $T(x)$ inside the reactor has been measured for various bed temperatures (Pielsticker et al., 2019). The effectiveness factor $\eta$ serves as a hydrodynamic compensation for the transition between PFR and CSTR behavior (Denbigh, 1944). Thus, the factor accounts for kinetic inefficiencies and non-ideal flow patterns. For the observed degrees of conversion, a factor $\eta = 1.3$ is assumed, meaning that the perfect PFR model would yield approximately 30 % higher conversions than the non-ideal reactor with the same reactor volume and fluid flow. Fig. 4 shows the temperature profile along the reactor axis and the corresponding local reactivity $r(x)$ for a reactor set temperature $T_{\mathrm{R}} = 873$ K.

In combination with the subsequently presented reaction kinetics, an effective reactor volume $V_{\mathrm{eff}} = 3.56 \times 10^{-4}$ m$^3$ was determined in an iterative procedure. Although the effective volume slightly depends (±15 %) on the kinetic mechanism and the reactor temperature, the effective reactor volume is kept constant for all cases to allow for a better comparison.

The differential equation to describe the conversion process in terms of the MMA concentration $c_{\mathrm{MMA}}$ along the $x$ coordinate in the PFR is given by

$$\frac{\partial(\dot{V} \cdot c_{\mathrm{MMA}})}{\partial x} = -A_{\mathrm{cross}} \cdot r_{\mathrm{tot}} \cdot c_{\mathrm{MMA}}, \tag{7}$$

where $\dot{V}$ is the volume flow corrected from the given volume flow under norm conditions set by the mass flow controllers, $A_{\mathrm{cross}}$ is the constant reactor cross-section, and $r_{\mathrm{tot}}$ is the total reaction rate given by the chemical decomposition mechanism.

In the present study, the chemical decomposition of MMA into smaller fragments is modeled via two different kinetic models: the single first-order reaction (SFOR) model and the two-competing-reactions model (CRM). In the SFOR model, the total kinetic rate is expressed as a single reaction via an Arrhenius approach

$$r_{\mathrm{SFOR}} = A \cdot \exp\left(-\frac{E_{\mathrm{a}}}{R \cdot T}\right) \tag{8}$$

with the two kinetic parameters activation energy $E_{\mathrm{a}}$ and pre-exponential factor $A$ as well as the universal gas constant $R$. In the CRM, the educt MMA is decomposed via two competing chemical reactions that sum to the overall reaction rate

$$r_{\mathrm{CRM}} = A_1 \cdot \exp\left(-\frac{E_{\mathrm{a},1}}{R \cdot T}\right) + A_2 \cdot \exp\left(-\frac{E_{\mathrm{a},2}}{R \cdot T}\right) \tag{9}$$

with two Arrhenius parameters for each reaction, summing up in four total parameters ($A_1$, $A_2$, $E_{\mathrm{a},1}$, and $E_{\mathrm{a},2}$). These parameters are determined by solving a minimization problem

$$\min_{A_i, E_{\mathrm{a},i}} \sum_i \left(\frac{y_{\mathrm{LG,mod,i}} - y_{\mathrm{LG,exp,i}}}{y_{\mathrm{LG,exp,i}}}\right)^2, \tag{10}$$

where the relative error between the modeled ($y_{\mathrm{LG,mod,i}}$) and experimental ($y_{\mathrm{LG,exp,i}}$) light gas yield is minimized in a least-squares procedure. In the model, the final light gas yield is obtained from the modeled concentration at the reactor outlet at length $L$

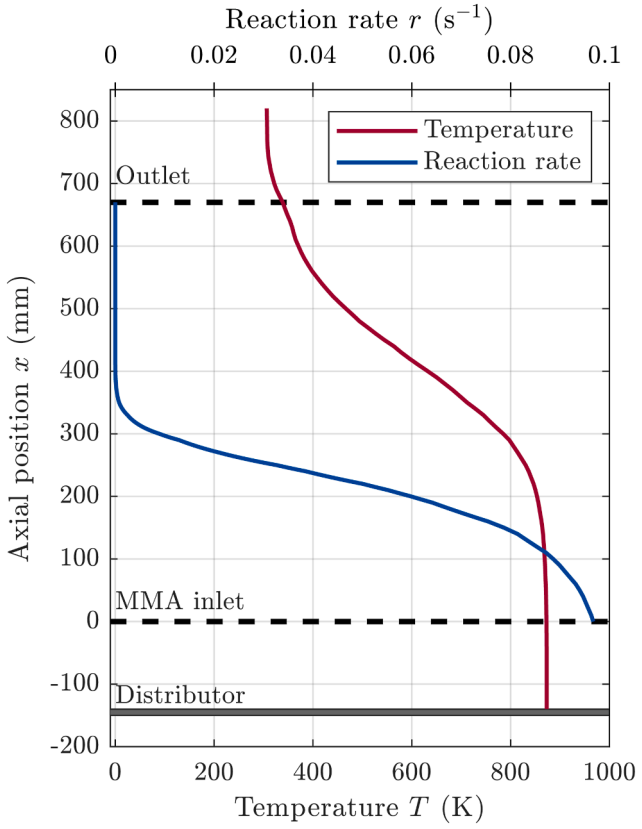


**Fig. 4.** Temperature profile along the reactor axis and corresponding local reaction rate for a reactor temperature $T_{\mathrm{R}} = 873$ K.

$$y_{\mathrm{LG,mod}} = 1 - \frac{c_{\mathrm{MMA}}(L)}{c_{\mathrm{MMA},0}}, \tag{11}$$

while the experimental one is determined as a sum of all measured species yields calculated by Eq. (4).

Alternatively to minimizing the relative error of the light gas yields, the reaction kinetic parameters for the SFOR model can be determined by an Arrhenius optimization, where the error between the calculated and experimentally obtained reaction rates is minimized:

$$\min_{A_i, E_{\mathrm{a},i}} \sum_i (r_{\mathrm{SFOR}} - r_{\mathrm{MMA}})^2 \tag{12}$$

For the combination of the plug flow reactor and the SFOR model, the reaction is

$$r_{\mathrm{MMA}} = -\frac{1}{\tau} \cdot \ln\left(\frac{\varphi_{\mathrm{MMA,FTIR}}}{\varphi_{\mathrm{MMA},0}}\right) = -\frac{1}{\tau} \cdot \ln(1 - y_{\mathrm{LG}}) \tag{13}$$

with $\tau$ being the gas residence time.

Due to the low initial volume fraction of MMA, the volume flow change due to the arising reaction products can be neglected, and thus, the residence time represents the ratio of the volume flow $\dot{V}_{\mathrm{N_2}}$ to the reactor volume $V$. As the determination of $r_{\mathrm{MMA}}$ from Eq. (13) is monovariate, errors in the determination of the light gas yield are directly transferred into the derived decomposition rate. For this reason, the error sensitivity of the problem is calculated using

$$\frac{\partial r_{\mathrm{MMA}}}{\partial y_{\mathrm{LG}}} = \frac{1}{\tau} \cdot \frac{1}{1 - y_{\mathrm{LG}}}. \tag{14}$$

Equation (14) shows that errors are damped with increasing residence time or reactor volume. However, the errors are amplified for high conversions once the light gas yield approaches $y_{\mathrm{LG}} = 1$. Consequently,

$r_{MMA}$ is determined this way only in a temperature range between 773 K and 973 K, where conversion is in the range 5−95 %.

Fig. 5 shows the experimentally obtained light gas yields in comparison with the predictions from the two different models, SFOR and CRM. In the SFOR model, a further distinction is made between the objective functions (Eq. (10) or (12)) used to determine the kinetic parameters. All sets can represent the general trend of increasing light gas formation with increasing residence time and temperature. However, differences in the accuracy and dependency on single quantities are visible. The SFOR model with parameters obtained by minimizing the error in the reaction rate tends to overpredict the decomposition in the middle temperature range between 823 and 908 K for all volume flows. While at lower and higher temperatures, the experimentally obtained conversion is higher than the model predictions. By determining the SFOR model parameters from a minimization of the relative yield error, it becomes obvious that there is a strong tendency to underpredict the conversion for high temperatures (especially 943 K). The CRM model can compensate for most of the inaccuracies obtained with the two SFOR model approaches. Especially, the volume flow dependency in the high-temperature regime is significantly improved, while maintaining the accuracy in the low-temperature region. Table 2 lists all determined kinetic parameters for the CRM and the SFOR model.

The SFOR model reaches identical activation energies independently of the objective function used. However, the pre-exponential factor determined by minimizing the error in the reaction rates via Eq. (12) is higher than those obtained from the minimization of the relative light gas yield (Eq. (10)), yielding approximately 50 % higher reaction rates. The effect is well shown in the Arrhenius diagram of the reaction rate depicted in Fig. 6.

The CRM reveals two reactions with significantly differing activation energies for both reactions. The ratio of the activation energies suggests that the radical fragmentation and cracking pathway has a higher activation energy ($E_{a,2}$) than the decarboxylation pathway leading to $CO_2$. A classification of the experimentally determined light gas species in products attributed to reaction 1 ($CO_2$, $CH_2O$, $CH_3OH$, and $C_2H_5OH$) and reaction 2 (CO, $CH_4$, $C_2H_6$, $C_2H_4$, $C_3H_8$, $C_3H_6$, $C_4H_{10}$, and $C_6H_6$) shows a high degree of consistency with the two corresponding CRM products as illustrated in Fig. 5. Only at higher temperatures, the reaction products from reaction 1 predicted by the CRM cannot totally cover the experimental yields. Most likely, $CO_2$ is not only a product of the decarboxylation reaction but also stems from the cracking pathway as verified in the study by Sanders et al. (2023). This confirms that two separate, parallel mechanisms are required to accurately model the overall decomposition.

### 3.3. Interplay of PMMA decomposition and MMA gas-phase reactions

Products obtained from the pyrolysis of solid PMMA particles are the result of the primary decomposition of the PMMA and the subsequent secondary reaction in the gas phase. The fundamental assumption commonly used in simplified models of PMMA pyrolysis is the two-step sequential decomposition approach. This model approach assumes that all initial polymer degradation leads exclusively to MMA monomer generation (depolymerization), and that all subsequent light gas formation (CO, $CO_2$, $CH_4$, etc.) results entirely from the secondary thermal cracking of the gaseous MMA monomer in the gas phase. However, this

**Table 2**
Kinetic parameters for the three MMA gas-phase decomposition model approaches. The term min $f(x)$ represents the objective function used to determine the kinetic parameters.

| Model | Pathway | $A$ [$s^{-1}$] | $E_a$ [kJ $mol^{-1}$] | min $f(x)$ |
|---|---|---|---|---|
| SFOR | Global | $1.84 \times 10^8$ | 155.5 | Eq. (12), $r$ |
| SFOR | Global | $1.23 \times 10^8$ | 155.0 | Eq. (10), $y_{LG}$ |
| CRM | Reac. 1 | $1.17 \times 10^3$ | 76.5 | Eq. (10), $y_{LG}$ |
| | Reac. 2 | $4.63 \times 10^{14}$ | 269.9 | |

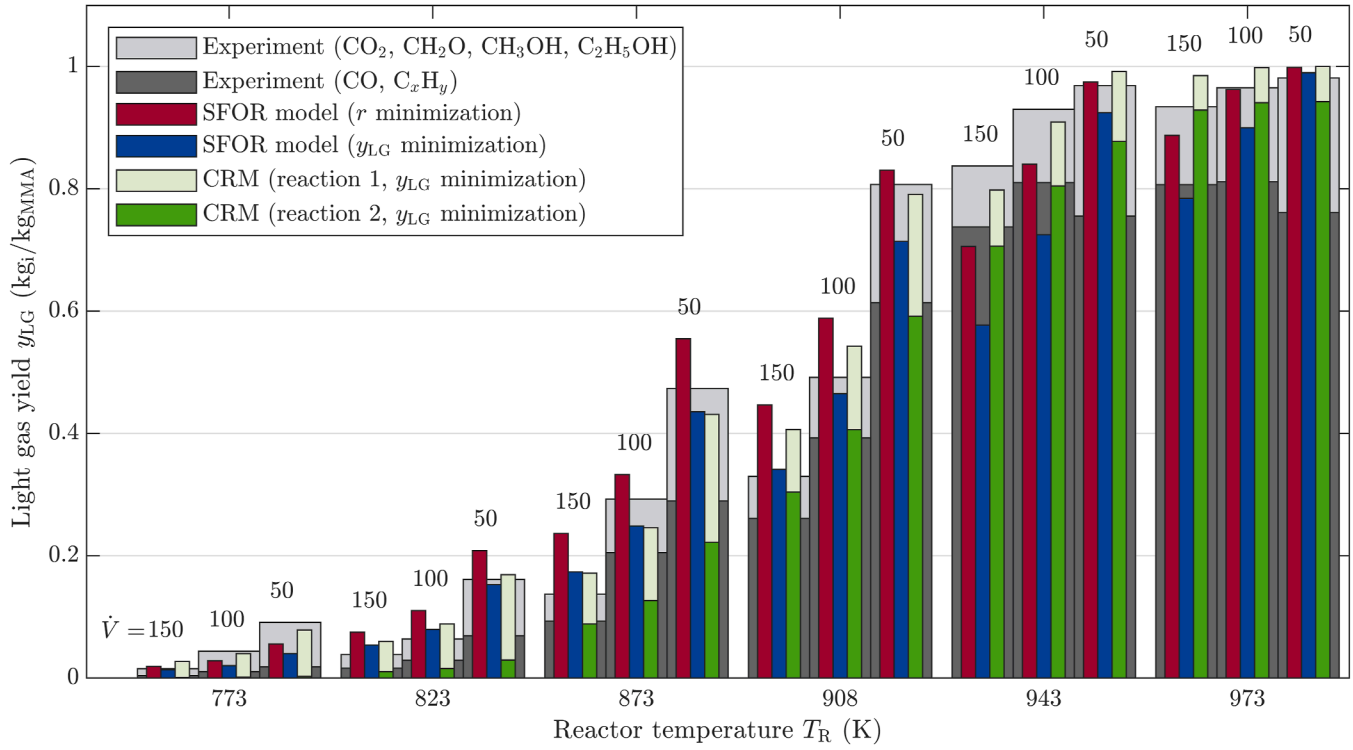


**Fig. 5.** Comparison of experimentally obtained light gas yields with model predictions from the single first-order (SFOR) model and the two-competing-reactions model (CRM) at different temperatures and volume flows. The experimental yields are classified according to the expected main reaction products of reactions 1 and 2 in the CRM. Numbers above the bars indicate the volume flow in liters per hour for norm conditions.

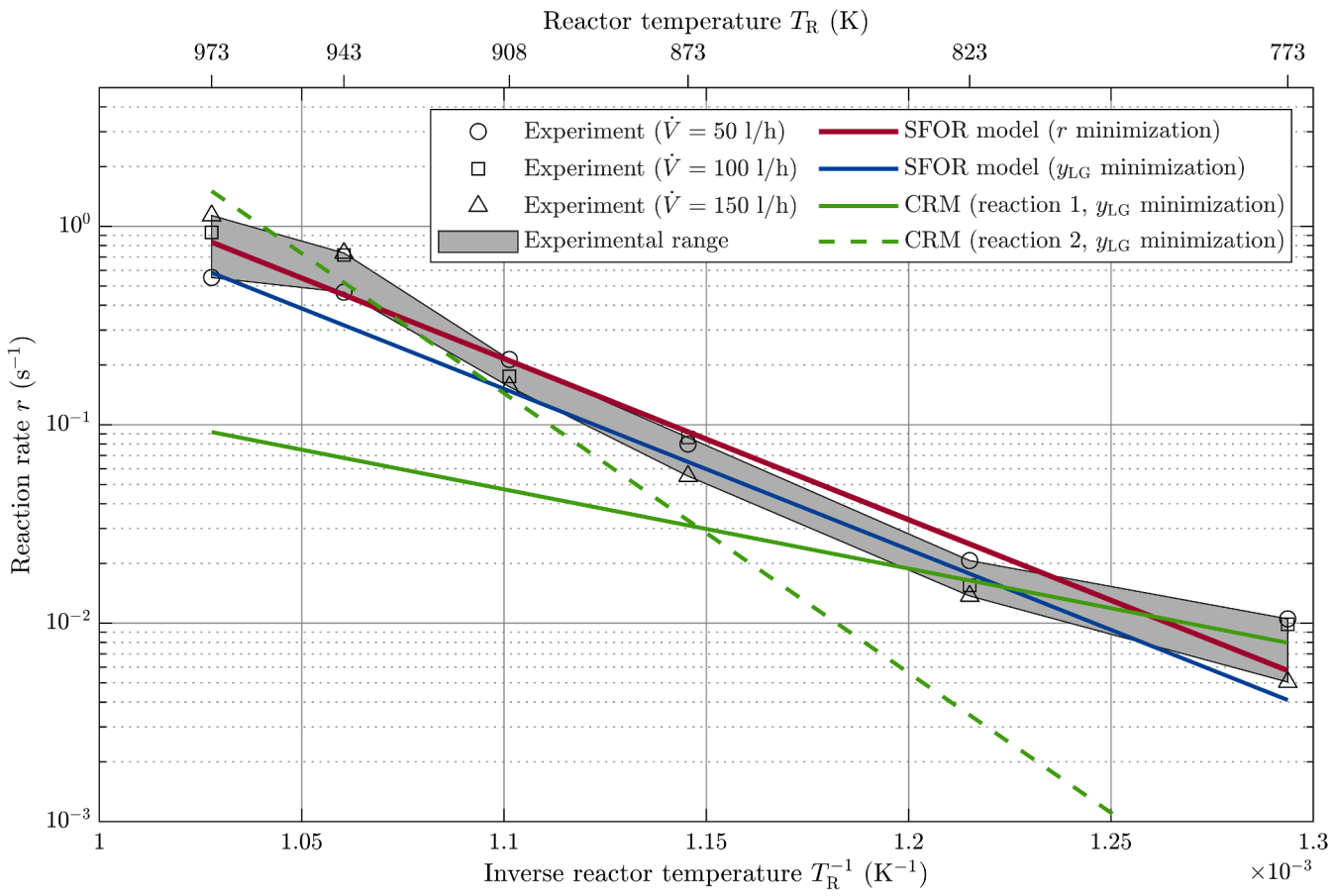


**Fig. 6.** Arrhenius diagram including experimentally obtained reaction rates for the gas-phase decomposition of MMA and derived Arrhenius kinetics for the global SFOR model (parameters either determined by minimizing the error in the reaction rate according to Eq. (12) or by minimizing the relative error in the light gas yield via Eq. (10)) and the CRM split up into the two competing reactions.

framework often overlooks the direct scission pathways occurring within the solid polymer matrix. Specifically, the model fails to adequately account for side-chain scission (breaking of the ester group, $COOCH_3$) and weak link scission (like head-to-head bonds), which occur in parallel with depolymerization (Holland & Hay, 2001; Moens et al., 2020). These direct pathways generate light gases and other volatile non-monomers – such as methanol and carbon dioxide (Moens et al., 2020) – independently of the MMA vapor cracking step. Neglecting this extra source of light gases from the primary solid-phase breakdown may lead to an underprediction of the total light gas yield and equally to an overprediction of the MMA yield.

The following investigation will analyze the interplay between primary and secondary pyrolysis reactions on the final yields of MMA and light gases. Fig. 7 shows the experimentally gained yields of MMA from the pyrolysis of PMMA particles examined in a previous study (Pielsticker et al., 2026). The temperature behavior of the MMA yield exhibits a biphasic trend, characterized by an initial increase to a maximum yield, followed by a sharp, monotonic decline in the high-temperature range. The overall mass balance reveals that for the lowest temperature, the degradation process is not completed within the experimental time of 32.6 min. The calculation by difference accounts for a PMMA yield of 12.5 % (marked as hatched area) and a light gas yield of 18.4 %. In contrast, complete conversion of PMMA has been detected at all other temperatures during the experimental time $t_{exp}$ used. Note that the experimental time is, in most cases, significantly longer than the conversion time to ensure that the entire conversion process is captured in the experiment. From the moderate MMA yield of 69.1 % at 623 K, the yield then undergoes a distinct increase to attain its maximum value at between 673 and 723 K around 90 %. Beyond 723 K, the trend reverses, showing a pronounced and monotonically decreasing relationship with rising temperature. From 723 to 873 K, the yield falls steadily. In the highest temperature range, spanning from 973 to 1073 K, the yield drops to 10 % or below, indicating near-total loss of the monomer product.

Fig. 8 illustrates multiple models to describe the primary conversion of PMMA ($SFOR_{PMMA}$ or $CRM_{PMMA}$) and the secondary conversion of MMA ($SFOR_{MMA}$ or $CRM_{MMA}$). Primary and secondary models are combined to describe the overall reaction mechanism from PMMA to light gas products. Besides the experimental data, Fig. 7 also includes the predictions of some of these model combinations.

The blue bars represent the single first-order reaction mechanism for PMMA decomposition ($SFOR_{PMMA}$), where only MMA is formed in the primary reaction step, and light gases result solely from the secondary gas-phase reaction ($SFOR_{MMA}$). Thus, this model combination ($SFOR_{PMMA} + SFOR_{MMA}$) reflects the classical sequential decomposition approach. This SFOR combination can capture the general temperature trend, however, it exhibits significant quantitative deviations from the experimental MMA yield at low temperatures (especially $T_R$ = 623 K, 36.9 %) and in the transition range between 773 and 873 K (20.0–82.1 %). In the temperature range from 673 to 773 K, the model predicts MMA yields above 96 %, which shows that the significance of gas phase reactions is of minor importance. Also, for temperatures below 773 K, the difference between the two gas-phase models is below 2 %. Consequently, this confirms that the sequential model is overlooking a pathway that consumes PMMA without producing MMA.

To address this kinetic deficiency, the established sequential decomposition from PMMA over MMA to light gas is extended by including a competing reaction pathway. The competing reaction model

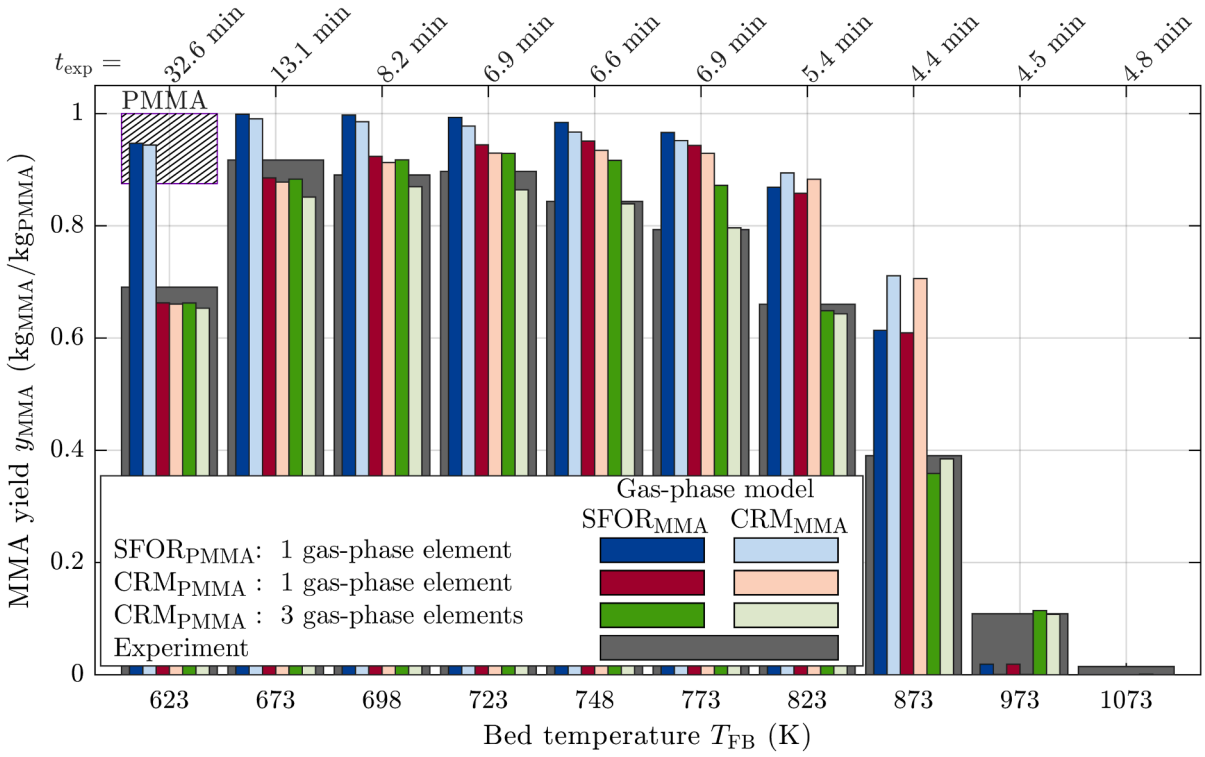


**Fig. 7.** Experimentally obtained MMA yields during the pyrolysis of solid PMMA particles at different reactor temperatures in comparison with model predictions using two primary pyrolysis models for the solid phase ($SFOR_{PMMA}$ and $CRM_{PMMA}$) and two models for the secondary gas-phase decomposition ($SFOR_{MMA}$ and $CRM_{MMA}$). The difference from 1 is the light gas yield except for $T_{FB}$ = 623 K, where the calculation by difference leads to a so far unreacted PMMA yield $y_{PMMA}$ = 0.12 at the given experimental time.

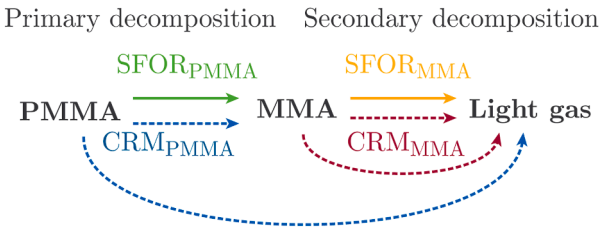


**Fig. 8.** Reaction schemes for the single first-order reaction (SFOR) model and the competing-reaction model (CRM) during the primary decomposition of PMMA and the subsequent secondary decomposition of MMA into light gas.

($CRM_{PMMA}$) incorporates a parallel degradation step where the solid PMMA is directly transferred to light gas, bypassing the MMA intermediate. The kinetic parameters for this newly introduced direct light gas formation pathway are directly taken from the low-temperature MMA decomposition kinetics previously established in the pure gas-phase MMA model. The reason for this is that in both cases, the cleavage of the side chain (the $COOCH_3$ group) is assumed to be the underlying mechanism, and thus a similar reaction characteristic can be assumed. Additionally, the MMA reactivity is decreased to match the same overall decomposition rate previously observed in the experiments (Pielsticker et al., 2026). As shown by the red bars, the ($CRM_{PMMA}$ achieves a substantial improvement in the predictivity compared to the $SFOR_{PMMA}$ + $SFOR_{MMA}$ combination. This improvement is most pronounced in the low-temperature regime ($T \leq 723$ K), where the model successfully addresses the large overprediction error (36.9 % at 623 K) of the purely sequential approach, validating the hypothesis that solid-phase side-chain scission contributes to light gas formation independently of the MMA intermediate. However, deficiencies remain primarily in the mid-to-high temperature range (773−973 K), where the model first continues to significantly overpredict the MMA yield (e.g., $y_{MMA,mod}$ = 0.61−0.71 predicted versus $y_{MMA,exp}$ = 0.39 experimental at 873 K) and then significantly underpredicts the MMA yield at 973 K. Since MMA formation dominates over direct light gas formation in this temperature range, no differences are detectable between the $SFOR_{PMMA}$ model (blue) and the $CRM_{PMMA}$ (red). Differences in the predicted MMA yields, therefore, depend only on the gas-phase model used and the underlying temperatures and gas residence times.

In the modelling of the two previous cases, the gas residence time is calculated by the volume flow (temperature corrected) and the volume of the reaction zone (fluidized bed). However, in the experiment, the formed gaseous species can mix with the gas in the freeboard above the bed. As the gas outlet is close to the bed, the gases in the freeboard are subject to significantly longer residence times. Although the purge gas flow coming from above is intended to minimize this effect, the increase in volume during the release of volatiles – especially during dosing and in the early reaction phase – can cause this volume flow to be insufficient, allowing reaction gases to enter the upper gas space.

It may also happen that the PMMA particles tend to float on the bed – as the Archimedes number of the PMMA particles ($Ar_{PMMA}$ = 414−1465) is significantly higher than those of the bed particles ($Ar_b$ = 17.6−62.4) – resulting in a shorter gas residence time for some components than if the entire volume of the fluidized bed is taken into account. Instead of one gas-phase volume, the third case (represented by green bars) assumes three gas-phase volumes with different gas residence times. Fig. 9 shows, schematically, areas within the reaction zone that could potentially result in longer or shorter residence times than the average residence time.

Since an exact calculation of the local residence time distribution requires more complex modelling approaches (e.g., computational fluid dynamics), the available reactor volume is arbitrarily split into three elements, representing shorter, average, and longer gas residence times. The split fraction of the total gas into the three elements and the relative residence time change are kept constant for all temperatures. Both

values are determined in a regression process, where the difference between model-predicted and experimental yields is minimized. The minimization reveals that approximately 65 % of the gases must be subject to a significantly longer residence time (factor 5−6.4), while 30 % underlie shorter residence times (factor 0.32−0.34). As already shown in an earlier study (Pielsticker et al., 2018), the gas-residence time distribution is shifted drastically towards larger residence times if mixing in the freeboard is not prevented. However, the residence time distribution calculated here reflects a potential scenario to explain the observed yields and should not be taken as a definitive measurement of the local hydrodynamic conditions.

The sequential refinement of the PMMA pyrolysis model – moving from the classical single-step approach to the final CRM with multiple gas volumes – demonstrates that high predictive accuracy requires the integration of both refined chemical kinetics and detailed reactor hydrodynamics. With this, the overall mean error can be reduced from 14 % (primary SFOR) over 9.5 % (primary CRM) to approximately 2 % (CRM with gas residence time distribution).

### 3.4. Optimal conditions for MMA recovery

Following the model validation step in section 3.3, the present section evaluates the MMA yield dependency in a wide parameter space regarding particle reaction time $t_p$, gas residence time $t_g$, and temperature $T$. This analysis provides fundamental insight into the dominating reaction steps and the derivation of optimum operation conditions for MMA recovery. Fig. 10 presents an overview of the predicted MMA yields from the pyrolysis of PMMA as a function of the two key times across nine different temperatures ranging from 500 to 900 K. For the prediction, the model combination of $CRM_{PMMA}$ and $CRM_{MMA}$ is used.

The surface plots reveal two well-known dependencies: At low temperatures, the primary decomposition process defines the relevant time to achieve full decomposition of the PMMA and thus reach maximum MMA yields. By contrast, at high temperatures, the gas residence time is the important parameter that controls the decomposition of the primary formed MMA into smaller light gas fragments. However, the initially available amount of MMA also depends on the temperature. Due to the kinetics of the competing reaction of MMA and light gas formation in the primary pyrolysis process, at very low temperatures, the light gas formation dominates, while at higher temperatures, the MMA formation pathway is favored. Reachable yields of MMA exceed a value of 90 % only for temperatures higher than 700 K independently of the gas residence time. To achieve high recovery rates, reaching this minimum temperature in the industrial process is evident. Increasing the temperature above 800 K does not offer any advantages in industrial applications, as the PMMA is already almost completely decomposed into MMA in the primary step, but decomposition increases with gas phase reactions as the temperature rises. While at 800 K the MMA yield is still above 90 % after 10 s, at 900 K it falls to only 20 % for the same gas residence time. In order to maintain an MMA yield above 90 %, the gas residence time must not exceed 1 s, which poses a challenge in large-scale industrial processes.

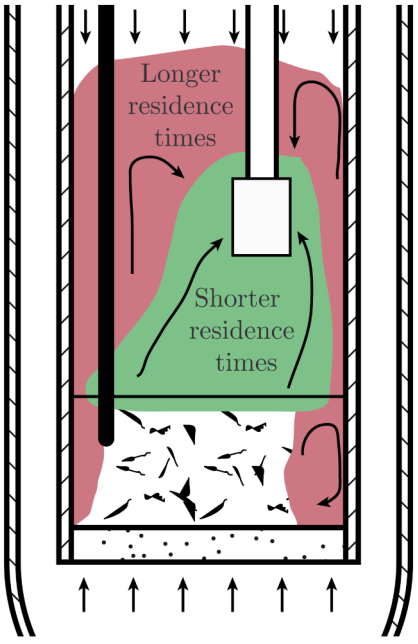


**Fig. 9.** Schematic representation of potential areas with shorter or longer gas residence times in the reaction zone.

The model-derived optimum temperature range of 700−750 K to achieve MMA yields above 95 % is strongly supported by experimental findings in the literature listed in Table 3.

The literature consensus for the optimal pyrolysis temperature is firmly proven to be in the range of 700−730 K, which precisely matches the model's optimum at 723 K. By adding catalysts to the reaction, the optimum temperature shifts towards lower temperatures (Chub et al., 2022). Multiple studies mention the reactor to be designed for the realization of short gas residence times, however, no study explicitly investigating different gas residence times and the impact on the MMA yield can be found.

## 4. Conclusion

This study successfully investigated the interplay between the solid-phase degradation and secondary gas-phase reactions to optimize polymethyl methacrylate thermal recycling in the context of methyl methacrylate recovery. The research followed a structured approach, initially focusing on the pyrolysis of pure methyl methacrylate (MMA) monomer in the gas phase. This step isolated the secondary decomposition kinetics and product formation pathways without the overlaying influence of the primary polymer decomposition. This fundamental understanding was then used to investigate the more complex reaction system of PMMA particles reacting inside a fluidized bed reactor, allowing for the comprehensive analysis of the combined primary (solid-phase) and secondary (gas-phase) reactions.

The experimental investigation of MMA gas-phase decomposition revealed that the product distribution of light gases is highly sensitive to temperature. This sensitivity dictates the final monomer yield. At temperatures below 700 K, the light gas output was dominated by carbon dioxide. Conversely, raising the temperature above 750 K significantly shifts the selectivity towards the formation of carbon monoxide (CO) and small $C_2$–$C_4$ hydrocarbons, indicating the strong dominance of high-intensity, MMA-reducing secondary decomposition reactions.

To accurately model this observed temperature-dependent selectivity, a two-competing-reactions model (CRM) was successfully implemented and validated against the experimental data. The two competing reactions are characterized by their distinct activation energies ($E_{a,1}$ = 76.5 kJ mol$^{-1}$ and $E_{a,2}$ = 269.9 kJ mol$^{-1}$), which reflect two parallel pathways: a lower-energy route that is dominant at low temperatures and favors stable products (e.g., $CO_2$), and a higher-energy route that governs the selectivity at high temperatures, yielding highly fragmented products (e.g., CO and $C_2$–$C_4$ hydrocarbons).

The findings obtained from the MMA investigation were then transferred to the more complex process of PMMA pyrolysis. The typical approach of modeling the decomposition of PMMA as a sequential reaction of PMMA into MMA and then further into light gas proved to be insufficient, primarily because direct light gas formation at low temperatures is not taken into account. The implementation of a competing direct light gas formation pathway with reaction kinetics observed from the pure MMA experiments significantly improved the model predictivity at low temperatures. The consideration of a multi-volume

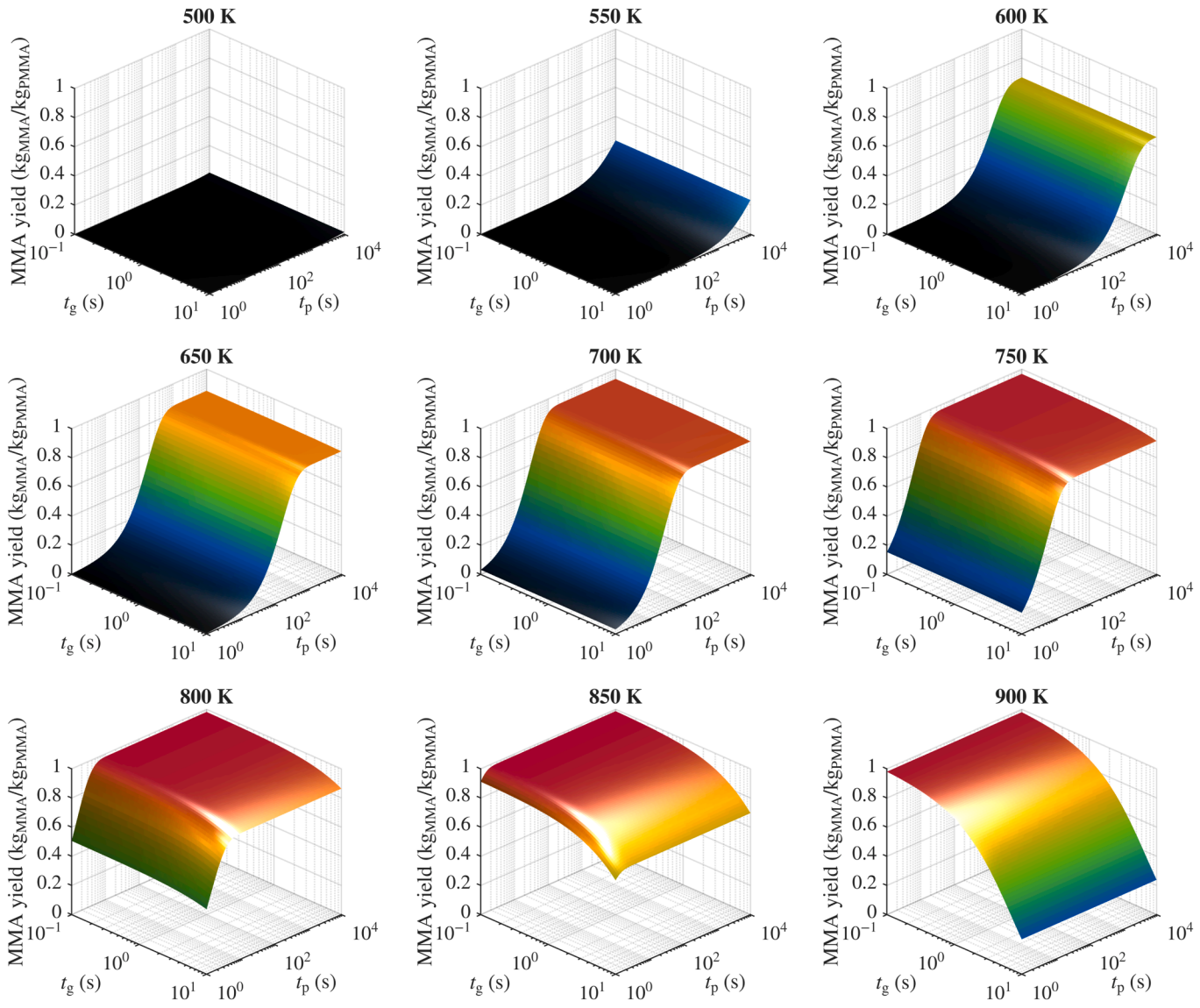


**Fig. 10.** Overview of achievable MMA yields as a function of particle reaction time and gas residence time at different reaction temperatures. Predictions result from the combination of $CRM_{PMMA}$ and $CRM_{MMA}$. Temperature for primary and secondary is assumed to be identical.

**Table 3**
Comparison of optimal PMMA pyrolysis temperature $T_{opt}$ for maximum monomer recovery $y_{MMA,max}$ from the literature and the model prediction.

| Reference | $T_{opt}$ [K] | $y_{MMA,max}$ [wt%] |
|---|---|---|
| Model prediction | 723 | >95 |
| Kaminsky & Franck, 1991 | 723 | 97.16 |
| Kang et al., 2008 | 713 | 96.6 |
| Ferreira et al., 2025 | 698 | 94.74 |

reaction model with different residence times has also shown that the interaction between PMMA and bed particles and the mixing behavior of the resulting gases with the freeboard is most likely more complex than can be represented by a simple one-volume model.

The newly developed framework allows for the prediction of the recoverable MMA yield considering effects of reaction temperature, particle reaction time, and gas-phase residence time. An optimum operation temperature to recover MMA yields above 95 % was identified at 723 K, matching observations in the literature exactly. This integrated modeling approach, which accurately links complex gas-phase kinetics with reactor-specific hydrodynamics, provides a vital framework for the rational design and optimization of industrial-scale polymer recycling processes. Ultimately, these findings enable precise control over operating parameters to maximize monomer yields. This significantly enhances the economic and environmental sustainability of chemical recycling processes.

## CRediT authorship contribution statement

**Stefan Pielsticker:** Writing – original draft, Visualization, Methodology, Formal analysis, Conceptualization. **Konstantinos Gfall:** Investigation, Formal analysis, Data curation. **Wilko Rohlfs:** Writing – review & editing, Supervision. **Reinhold Kneer:** Writing – review & editing, Supervision, Project administration, Funding acquisition.

## Declaration of competing interest

The authors declare that they have no known competing financial interests or personal relationships that could have appeared to influence the work reported in this paper.

## Acknowledgement

The authors thank the funding from the Exploratory Research Space – ERS, RWTH Aachen under grant agreement PFKA008 “Cluster 4 Plastics Recycling” and the German Research Foundation (DFG) — project number 215035359 — within the CRC/TRR 129 “Oxyflame”.

## Data availability

All data obtained in this study are available open access. This includes the experimental data from the MMA (DOI: 10.18154/RWTH-2026-04902) and the PMMA experiments (DOI: 10.18154/RWTH-2026-03676).

## References

Abad, A., Cardona, S. C., Torregrosa, J. I., López, F., & Navarro-Laboulais, J. (2005). Flow analysis deconvolution for kinetic information reconstruction. *Journal of Mathematical Chemistry, 38*, 271–292. https://doi.org/10.1007/s10910-005-5422-8

Achilias, D. S. (2007). Chemical recycling of poly(methyl methacrylate) by pyrolysis. Potential use of the liquid fraction as a raw material for the reproduction of the polymer. *European Polymer Journal, 43*, 2564–2575. https://doi.org/10.1016/j.eurpolymj.2007.02.044

Arisawa, H., & Brill, T. B. (1997). Kinetics and mechanisms of flash pyrolysis of poly (methyl methacrylate) (PMMA). *Combustion and Flame, 109*, 415–426. https://doi.org/10.1016/S0010-2180(96)00190-3

Blanco, M. B., Bejan, I., Barnes, I., Wiesen, P., & Teruel, M. A. (2014). Products and mechanism of the reactions of OH radicals and Cl atoms with methyl methacrylate (CH2=C(CH3)C(O)OCH3) in the presence of NOx. *Environmental science & technology, 48*, 1692–1699. https://doi.org/10.1021/es404771d

Braido, R. S., Borges, L. E. P., & Pinto, J. C. (2018). Chemical recycling of crosslinked poly(methyl methacrylate) and characterization of polymers produced with the recycled monomer. *Journal of Analytical and Applied Pyrolysis, 132*, 47–55. https://doi.org/10.1016/j.jaap.2018.03.017

Brockhaus, V. A., & Jenckel, E. (1956). Über die Kinetik des thermischen Abbaues von Polymethacrylsäuremethylester. *Makromolekulare Chemie, 18*, 262–293. https://doi.org/10.1002/macp.1956.020180124

Chub, O. V., Saadatkhah, N., Dubois, J.-L., & Patience, G. S. (2022). Fluidized bed poly (methyl methacrylate) thermolysis to methyl methacrylate followed by catalytic hydrolysis to methacrylic acid. *Applied Catalysis A: General, 638*, Article 118637. https://doi.org/10.1016/j.apcata.2022.118637

Dakshnamurthy, S., Knyazkov, D. A., Dmitriev, A. M., Korobeinichev, O. P., Nilsson, E. J., Konnov, A. A., & Narayanaswamy, K. (2019). Experimental study and a short kinetic model for high-temperature oxidation of methyl methacrylate. *Combustion Science and Technology, 191*, 1789–1814. https://doi.org/10.1080/00102202.2018.1535492

Denbigh, K. G. (1944). Velocity and yield in continuous reaction systems. *Transactions of the Faraday Society, 40*, 352. https://doi.org/10.1039/TF9444000352

dos Santos, P. B., Da Ribeiro, H. J. S., Ferreira, A. C., Ferreira, C. C., Bernar, L. P., Da Assunção, F. P. C., de Castro, D. A. R., Santos, M. C., Duvoisin, S., Borges, L. E. P., & Machado, N. T. (2022). Process analysis of PMMA-based dental resins residues depolymerization: Optimization of reaction time and temperature. *Energies, 15*, 91. https://doi.org/10.3390/en15010091

Ferreira, A. C., Da Ribeiro, H. J. S., de Castro, D. A. R., Santos, M. C., Ferreira, C. C., Da Assunção, F. P. C., Duvoisin, S., Pizarro Borges, L. E., Teixeira Machado, N., & Bernar, L. P. (2025). Process analysis of PMMA dental waste depolymerization in semi-batch reactors. *Polymers, 17*. https://doi.org/10.3390/polym17192711

Ferriol, M., Gentilhomme, A., Cochez, M., Oget, N., & Mieloszynski, J. L. (2003). Thermal degradation of poly(methyl methacrylate) (PMMA): Modelling of DTG and TG curves. *Polymer Degradation and Stability, 79*, 271–281. https://doi.org/10.1016/S0141-3910(02)00291-4

Geldart, D. (1973). Types of gas fluidization. *Powder Technology, 7*, 285–292. https://doi.org/10.1016/0032-5910(73)80037-3

Gfall, K., Kneer, R., & Pielsticker, S. (2025). Determination of PMMA pyrolysis kinetics and the role of heat transfer limitations. In *13th Mediterranean Combustion Symposium*. https://publications.rwth-aachen.de/record/1012613.

Gkaliou, K., Benedini, L., Sárossy, Z., Dalsgaard Jensen, C., Henriksen, U. B., & Daugaard, A. E. (2023). Recycled PMMA prepared directly from crude MMA obtained from thermal depolymerization of mixed PMMA waste. *Waste Management, 164*, 191–199. https://doi.org/10.1016/j.wasman.2023.04.007

Holland, B. J., & Hay, J. N. (2001). The kinetics and mechanisms of the thermal degradation of poly(methyl methacrylate) studied by thermal analysis-Fourier transform infrared spectroscopy. *Polymer, 42*, 4825–4835. https://doi.org/10.1016/S0032-3861(00)00923-X

Kaminsky, W., & Franck, J. (1991). Monomer recovery by pyrolysis of poly(methyl methacrylate) (PMMA). *Journal of Analytical and Applied Pyrolysis, 19*, 311–318. https://doi.org/10.1016/0165-2370(91)80052-A

Kang, B.-S., Kim, S. G., & Kim, J.-S. (2008). Thermal degradation of poly(methyl methacrylate) polymers: Kinetics and recovery of monomers using a fluidized bed reactor. *Journal of Analytical and Applied Pyrolysis, 81*, 7–13. https://doi.org/10.1016/j.jaap.2007.07.001

Kashiwagi, T., Inaba, A., Brown, J. E., Hatada, K., Kitayama, T., & Masuda, E. (1986). Effects of weak linkages on the thermal and oxidative degradation of poly(methyl methacrylates). *Macromolecules, 19*, 2160–2168. https://doi.org/10.1021/ma00162a010

Kikuchi, Y., Hirao, M., Ookubo, T., & Sasaki, A. (2014). Design of recycling system for poly(methyl methacrylate) (PMMA). Part 1: Recycling scenario analysis. *International Journal of Life Cycle Assessment, 19*, 120–129. https://doi.org/10.1007/s11367-013-0624-y

Korobeinichev, O. P., Paletsky, A. A., Gonchikzhapov, M. B., Glaznev, R. K., Gerasimov, I. E., Naganovsky, Y. K., Shundrina, I. K., Snegirev, A. Y., & Vinu, R. (2019). Kinetics of thermal decomposition of PMMA at different heating rates and in a wide temperature range. *Thermochimica Acta, 671*, 17–25. https://doi.org/10.1016/j.tca.2018.10.019

Kunii, D., & Levenspiel, O. (1997). Circulating fluidized-bed reactors. *Chemical Engineering Science, 52*, 2471–2482. https://doi.org/10.1016/S0009-2509(97)00066-3

Moens, E. K. C., de Smit, K., Marien, Y. W., Trigilio, A. D., van Steenberge, P. H. M., van Geem, K. M., Dubois, J.-L., & D'hooge, D. R. (2020). Progress in reaction mechanisms and reactor technologies for thermochemical recycling of poly(methyl methacrylate). *Polymers, 12*. https://doi.org/10.3390/polym12081667

Nguyen, T. D., Saadatkhah, N., Zhuang, Y., de Tommaso, J., Stoeffler, K., Faye, A., & Patience, G. S. (2026). Thermal degradation of impact–modified PMMA in mechanical and chemical recycling. *Canadian Journal of Chemical Engineering, 104*, 31–43. https://doi.org/10.1002/cjce.70004

NIST chemistry WebBook: Methyl methacrylate. URL: https://webbook.nist.gov/cgi/cbook.cgi?ID=++80-62-6, (2023).

OECD. (2022). *Global plastics outlook: Economic drivers, environmental impacts and policy options*. Paris: OECD Publishing. https://doi.org/10.1787/de747aef-en

Pielsticker, S., Gfall, K., Solana Gómez, R., Kneer, R., & Rohlfs, W. (2026). Reaction kinetics versus transport mechanisms: Assessing the rate-limiting factor in high-temperature PMMA pyrolysis for chemical recycling. *Fuel*. https://doi.org/10.1016/j.fuel.2026.139902

Pielsticker, S., Hendricks, K., & Kneer, R. (2024). *Fourier-transform infrared (FTIR) spectra of gaseous methyl methacrylate (MMA)*. https://doi.org/10.18154/RWTH-2024-08098

Pielsticker, S., Hendricks, K., Knevels, C., Lehnertz, M. S., Palkovits, R., & Kneer, R. (2025). Experimental determination of quantitative yields from polymethyl methacrylate (PMMA) flash pyrolysis in a fluidized bed reactor via online FTIR gas analysis. *Fuel, 392*, Article 134827. https://doi.org/10.1016/j.fuel.2025.134827

Pielsticker, S., Möller, G., Gövert, B., Kreitzberg, T., Hatzfeld, O., Yönder, Ö., Angenent, V., Hättig, C., Schmid, R., & Kneer, R. (2018). Influence of biomass torrefaction parameters on fast pyrolysis products under flame-equivalent conditions. *Biomass and Bioenergy, 119*, 392–410. https://doi.org/10.1016/j.biombioe.2018.08.014

Pielsticker, S., Schlögel, K. U., Kreitzberg, T., Hatzfeld, O., & Kneer, R. (2019). Biomass pyrolysis kinetics in a fluidized bed reactor: Measurements and plausibility verification for reaction conditions. *Fuel, 254*, Article 115589. https://doi.org/10.1016/j.fuel.2019.05.172

Sanders, I. C., Kuenning, N. M., Minesi, N. Q., Pineda, D. I., & Spearrin, R. M. (2023). Methyl methacrylate thermal decomposition: Modeling and laser spectroscopy of species time-histories behind reflected shock waves. *Fuel, 335*, Article 126846. https://doi.org/10.1016/j.fuel.2022.126846

Smolders, K., & Baeyens, J. (2004). Thermal degradation of PMMA in fluidised beds. *Waste Management, 24*, 849–857. https://doi.org/10.1016/j.wasman.2004.06.002

Zeng, W. R., Li, S. F., & Chow, W. K. (2002). Review on chemical reactions of burning poly(methyl methacrylate) PMMA. *Journal of Fire Sciences, 20*, 401–433. https://doi.org/10.1177/0734904102020005482